Random blebbing motion: A simple model linking cell structural properties to migration characteristics

Thomas E. Woolley
Cardiff School of Mathematics Cardiff University Senghennydd Road, Cardiff, CF24 4AG, United Kingdom

Eamonn A. Gaffney and Alain Goriely
University of Oxford, Andrew Wiles Building, Radcliffe Observatory Quarter, Woodstock Road, Oxford, OX2 6GG, United Kingdom

(Received 9 April 2017; published 18 July 2017)

If the plasma membrane of a cell is able to delaminate locally from its actin cortex, a cellular bleb can be produced. Blebs are pressure-driven protrusions, which are noteworthy for their ability to produce cellular motion. Starting from a general continuum mechanics description, we restrict ourselves to considering cell and bleb shapes that maintain approximately spherical forms. From this assumption, we obtain a tractable algebraic system for bleb formation. By including cell-substrate adhesions, we can model blebbing cell motility. Further, by considering mechanically isolated blebbing events, which are randomly distributed over the cell, we can derive equations linking the macroscopic migration characteristics to the microscopic structural parameters of the cell. This multiscale modeling framework is then used to provide parameter estimates, which are in agreement with current experimental data. In summary, the construction of the mathematical model provides testable relationships between the bleb size and cell motility.

DOI: 10.1103/PhysRevE.96.012409

I. INTRODUCTION

Cells are often produced away from the locations where they are needed [1–4]. In order to fulfill their role, cells need to sense their environments and migrate to their target area. Migration can occur passively through such mechanisms as population pressure arising from cell proliferation and loss or through the global movement of extracellular matrix components akin to a conveyor belt action [5–7]. Here, we are interested in how active motion is generated via dynamic conformational changes in cellular shape [8–10].

We focus our attention on exploring the interplay between shape and motion in a specific form of cellular deformation known as blebbing. Blebs are cellular protrusions that occur when the membrane delaminates from the actin cortex [11]. This released membrane balloons out into a hemispherical protrusion, which is driven by the intercellular pressure being larger than the extracellular pressure [12]. Over the course of 10–30 s the bleb's growth is arrested and the bleb enters a stationary phase. During this phase, a cortex is reformed in the blebbed expansion leading to a slower retraction phase of about 2 min, over which time the membrane and cortex are retracted back into the cell [13]. At this point, the blebbing cycle can begin again.

Blebs play an important role in a number of diverse processes in cellular biology, including mitosis and locomotion, and across a wide range of cell types, such as tumor cells, embryonic cells, and stem cells [13–18]. Since the membrane is flexible, blebs can take many forms. Here we focus on a rather ubiquitous type that are highly rounded and spherical (see Fig. 1) [18–23]. Our present investigation considers muscle satellite stem cells, which use blebs to migrate along muscle fibers in order to find and repair sites of muscle damage. Critically, it has been demonstrated experimentally that if a satellite cell's blebs are too big, or too small, the cell does not move effectively [24].

It should be noted that, since our results depend on fixing the geometry of the problem to be spherical, tubular and other bleb shapes [25] are outside the scope of our applicability. Further, we are assuming that the majority of the blebs are mechanically isolated as seen in Fig. 1. Other cells produce multiple small blebs continuously on top of one another [18]; once again, these are outside the scope of our results.

Blebbing, and the migration that it produces, has received a lot of attention recently from the mathematical modeling community and, thus, there are a number of different frameworks [20,26] that span a huge range of complexity [27,28]. Due to the blebbing process being so intricate, it is often necessary to use highly detailed models to reproduce observed results. For example, in previous studies we have shown that the neck of a bleb must be highly controlled to stop membrane excessively tearing away from cortex [29]. Equally, the shrinking rates of the membrane and cortex must be carefully tuned if the cell is to complete its retraction stage [30]. However, if details about the neck region are not needed, then simpler models considering the membrane and cortex as a composite material can be used to approximate the full biological complexity [31]. Moreover, due to the spherical shape of the cell and blebs, solid mechanical models of the membrane and cortex can be simplified by fixing the geometry of the bodies and treating the system as a set of coupled spherical caps [32].

In this paper, we aim to derive a parsimonious model that captures the generic features of muscle satellite stem cell and link the observable movement characteristics of this cell type [13] back to a simple geometric description, allowing us to predict parameter regions for variables that are difficult to calculate experimentally and to assess how cell properties impact on blebbing motility. Critically, what we lose in terms of accuracy is compensated for in terms of generalizability and simplicity. Our model considers a full three-dimensional blebbing cell that can undergo multiple blebbing events over its entire surface, as well as interact with and adhere to a flat two-dimensional substrate and, thus, generate movement. The motion occurs through the production of point adhesions from the blebs and the cell rolling onto the blebs during retraction.

 ©2017 American Physical Society

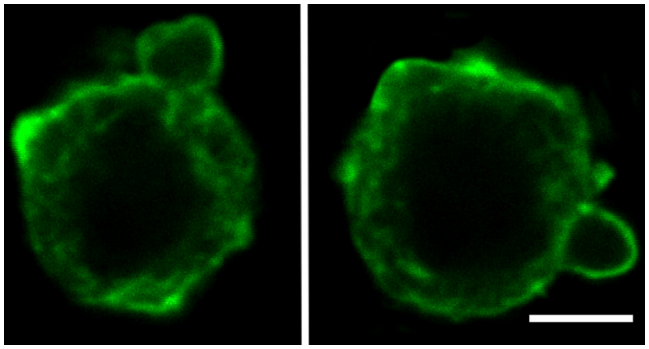

FIG. 1. A blebbing muscle stem cell with fluorescent actin skeleton at two different time points, illustrating the rounded form of the cells and blebs. Used with permission from the Skeletal Muscle Development Group, University of Reading. Scale bars, 5 μm.

We note that this is only one form of bleb migration. Indeed, blebbing cells have been seen to be very good at expanding protrusions into, and squeezing through, gaps, to navigate crowded environments [19,28]. However, this is not seen in stem cell motion along muscle fibers. Equally, other cells are seen to have large contact surfaces [33] due to the cell spreading over the substrate. Critically, from the movies of Collins-Hooper *et al.* [13], not only do we see that muscle stem cell motion remains extremely spherical throughout the migration, but also the motion appears to arise from a rolling phenomenon, whereby the blebs pulling the cell in a given direction [24]. Cells that bleb with long lobopodia, or flatter protrusions, are outside the scope of the current model

We begin in Sec. II by introducing the general solid mechanics formulation in terms of differential equations on the domain of the membrane. This formulation is simplified in Sec. II A to an analytical framework and extended in Sec. II B to include adhesive coupling to a flat substrate. In Sec. II C, we assume that the blebs are uniformly random and derive relationships for the probability density functions detailing the stochastics of cell displacement due to blebbing. These results are illustrated in Sec. III, where we demonstrate the link between experimental data of cellular motion and structural properties of the cell, before summarising our findings in Sec. IV.

II. MODEL

We begin with a brief summary of the solid mechanics model (see Ref. [29] for a more in-depth discussion) and then demonstrate how fixing the geometry of the components to those of spherical caps simplifies the formulation.

The fundamental set of equations defining the axisymmetric geometry of the problem is

$$\frac{\partial y}{\partial \sigma} = \lambda_s \cos(\theta), \tag{1}$$

$$\frac{\partial \theta}{\partial \sigma} = \lambda_s \kappa_s, \tag{2}$$

$$\frac{\partial z}{\partial \sigma} = -\lambda_s \sin(\theta), \tag{3}$$

$$\frac{\partial s}{\partial \sigma} = \lambda_s. \tag{4}$$

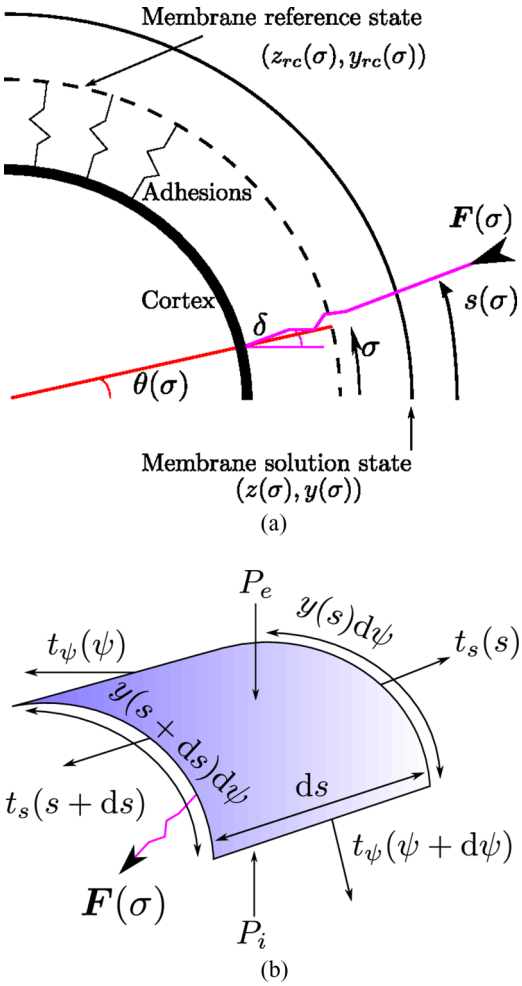

FIG. 2. Schematic diagram of stresses acting on the membrane of the cell. (a) Definition of adhesion forces and geometric variables. (b) Adhesion forces, surface tensions, and cellular pressures defined on a small section of the membrane. Variable definitions: (z_{rc}, y_{rc}), reference configuration of the membrane; (z, y), solution position of the membrane; σ, reference configuration arc length; s, solution configuration arc length; θ, angle normal to membrane solution configuration; $\boldsymbol{F}$, Force vector produced by adhesions; δ, angle of adhesion action; t_s and t_ψ, surface tensions; P_e and P_i, external and internal cell pressures, respectively. For further details, see text.

The model is rotationally symmetric about the z axis and the azimuthal angle is denoted ψ (see Fig. 2). The y and z variables are the Cartesian coordinates of the solution configuration, representing the shape of an unstressed Cartesian reference configuration, $(z_{\rm rc}, y_{\rm rc})$, once it has been pressurized by a pressure difference, ΔP. In our case, the initial reference configuration is a single sphere of radius ρ_c, which will be broken into spherical caps once blebs are allowed to occur. The arc length, σ, of the reference configuration (measured from the intercept of the reference configuration with the z axis) is used to parameterise the system. The solution and reference configurations are related via the *arc length stretch ratio*, λ_s [defined by Eq. (4)], which characterizes the local stretching of the body coordinates with respect to arc length

and the *radial stretch ratio*,

$$\lambda_\psi = \frac{y(\sigma)}{y_{\rm rc}(\sigma)}, \tag{5}$$

which measures the axisymmetric deformation. Finally, κ_s [defined by Eq. (2)] and

$$\kappa_\psi = \frac{\sin(\theta)}{y} \tag{6}$$

are the principal curvatures of an axisymmetric surface along the arc length and along the azimuthal angle, respectively, where θ is the normal angle of the membrane.

Having defined the geometry, we define the force balances through the equations

$$\frac{\partial(y t_s)}{\partial\sigma} = \lambda_s[t_\psi \cos(\theta) + F(\sigma) C y \sin(\delta - \theta)], \tag{7}$$

$$\Delta P = [\kappa_\psi t_\psi + \kappa_s t_s + F(\sigma) C \cos(\delta - \theta)], \tag{8}$$

where the surface tensions, t_s and t_ψ, are coupled to the strains through large extension constitutive laws,

$$t_s = A\left[\lambda_s^2 + \mu\left(\frac{y}{y_{\rm rc}}\right)^2 - (1+\mu)\right], \tag{9}$$

$$t_\psi = A\left[\mu\lambda_s^2 + \left(\frac{y}{y_{\rm rc}}\right)^2 - (1+\mu)\right]. \tag{10}$$

The parameter μ measures the relative extensibility of the membrane in the azimuthal and longitudinal directions, while the parameter A characterizes the elastic properties of the membrane [34].

The adhesion force, $F(\sigma) = |\boldsymbol{F}(\sigma)|$, is given by

$$F(\sigma) = \kappa E(\sigma) H[E_c - E(\sigma)], \tag{11}$$

$$E(\sigma) = \{\sqrt{[z(\sigma) - R_c\cos(\sigma/\rho_c)]^2 + [y(\sigma) - R_c \sin(\sigma/\rho_c)]^2} - (\rho - R_c)\}. \tag{12}$$

The adhesions couple the material points of the membrane and cortex, while the force is assumed to act along the line connecting these two points. The cortex is assumed to be a sphere of radius R_c that is concentric with the reference configuration; thus, initially the adhesions are all connected along the radial trajectories, normal to the cortex. Although not explicitly modeled here, cortical tension is, no doubt, an important factor controlling the terminal size of the blebs. A constitutive relationship linking cortex tension and pressure could be added to the model to provide an implicit account of cortex tension. However, on account of not having such data, we focus on specifying the pressure directly.

The adhesions are modeled as piecewise Hookean springs with spring constant κ [35]. Note that κ is measured per adhesion; thus, it is multiplied by an adhesion concentration, C, to provide a force per unit area, which opposes the pressure gradient. Note that the force is linearly related to the extension up until a critical extension, E_c, beyond which we assume that the adhesions break. This is enforced by the Heaviside function $H[E_c - E(\sigma)]$ in Eq. (11). Finally, as the membrane evolves the adhesions will move and, thus, δ is the angle along which the force is directed, where

$$\tan(\delta) = \frac{y(\sigma) - R_c \sin(\sigma/\rho_c)}{z(\sigma) - R_c\cos(\sigma/\rho_c)}. \tag{13}$$

A. Geometric enforcement

Enforcing the geometric constraint that the shell remains spherical throughout greatly simplifies these equations. Substituting the expression $(z, y) = (r_c\cos(\theta), r_c\sin(\theta))$ into Eqs. (1)–(13), we quickly find that the system reduces to

$$\kappa_s = \kappa_\phi = \frac{1}{r_c}, \tag{14}$$

$$\lambda_s = \lambda_\phi = \frac{r_c}{\rho_c}, \tag{15}$$

$$t_s = t_\phi = A(1+\mu)\left[\left(\frac{r_c}{\rho_c}\right)^2 - 1\right], \tag{16}$$

$$\theta = \frac{\sigma}{\rho_c}, \tag{17}$$

$$F = \kappa(r_c - \rho_c), \tag{18}$$

$$r_c(\Delta P - FC) = 2t_s. \tag{19}$$

Whence, we find the radius of the initial spherical solution, r_{c0}, in terms of the parameters: $C\kappa$, the adhesion strength density; ΔP_0, the initial pressure difference; ρ_c, the reference radius; μ, the relative extensibility of the membrane; and A, the membrane stiffness, via Eqs. (16), (18), and (19),

$$r_{c0} = \frac{(C\kappa\rho_c + \Delta P_0)\rho_c^2 + \sqrt{(C\kappa\rho_c + \Delta P_0)^2 \rho_c{}^4 + 8A(1+\mu)[C\kappa\rho_c^2 + 2A(1+\mu)]\rho_c^2}}{2C\kappa\rho_c^2 + 4A(1+\mu)}. \tag{20}$$

Note that because the membrane can only stretch 4% before lysis occurs [36], we expect $r_{c0} \approx \rho_c$. Using Eqs. (16), (18), and (19), once again, we can provide the linear estimate, with respect to $\epsilon = r_{c0}/\rho_c - 1 \ll 1$,

$$r_{c0} \approx \rho_c\left[1 + \frac{\Delta P_0 \rho_c}{C\kappa\rho_c^2 + 4A(\mu+1) - \Delta P_0 \rho_c}\right], \tag{21}$$

which makes the parameter dependencies much more obvious. Note that, although the denominator can be set to zero through judicious choice of parameter values, in the case we are considering,

$$C\kappa\rho_c^2 + 4A(\mu+1) \gg \Delta P_0 \rho_c, \tag{22}$$

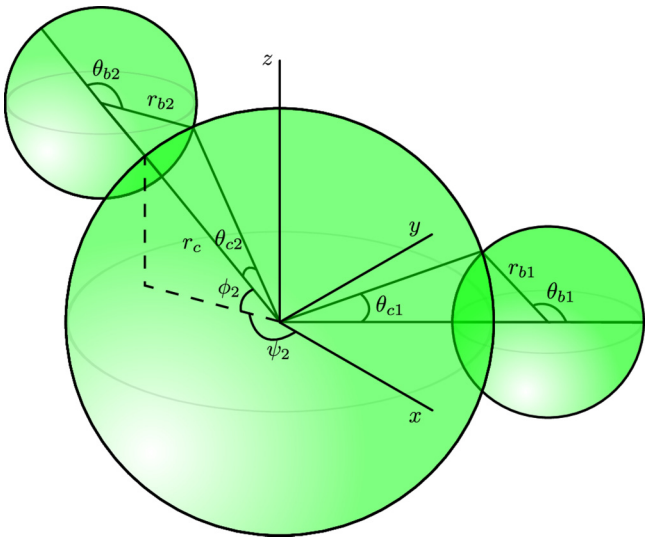

FIG. 3. Schematic diagram illustrating the bleb and cell geometry. For the ith bleb we define the variables: r_{bi}, bleb radius; θ_{bi}, neck opening angle of bleb; (ϕ_i, ψ_i), polar angles denoting the bleb's position; θ_{ci}, neck opening angle of cell.

and, hence, no singularity develops. It should also be noted that inequality Eq. (22) also suggests that the radius is approximately linear in ΔP_0.

From this we can calculate the initial volume of the spherical cell, $V = 4\pi r_{c0}^3/3$, in terms of ΔP_0 and other parameters. During blebbing, the total volume contained within the blebs and main cell body remains constant. Thus, the pressure difference, ΔP, is used as a Lagrange multiplier, enforcing this requirement. Specifically, as a bleb grows the internal pressure is released, decreasing ΔP. In turn, this reduction in pressure reduces the volume of the cell body, as well as the maximum size to which the bleb can grow, to ensure that the volume constraint is satisfied.

Equations (14)–(19) are also true for spherical caps, so, we can extend the system beyond the initial simple spherical cell to include blebbed states, where the cell and bleb are coupled through the global pressure difference and volume constraint. Note that by extending the system to include blebs, not only do we need to specify the radius of the cell and the bleb, r_c and r_b, respectively, but we also need to specify the cell and bleb neck angles that connect the two components (see Fig. 3). It should be noted that although the equations, as derived here, take into account any number of blebs, later we will restrict the model to single, mechanically isolated blebs. More generally, given a cell of radius r_c, from which the ith bleb expands with a neck angle of θ_{ci}, we define the reference configuration radius of the bleb to be ρ_{bi}, the solution radius of the bleb to be r_{bi}, and the bleb neck angle to be θ_{bi} (see Fig. 3). Finally, define a set $\mathbb{A}$, to contain the indices, i, of the active blebs, i.e., blebs that have not been fully retracted. From these definitions we derive the following system:

$$V = \frac{4}{3}\pi r_0^3 = V_c + \sum_{i\in\mathbb{A}} V_{bi}, \tag{23}$$

$$V_c = \frac{4}{3}\pi r_c^3 - \sum_{i\in\mathbb{A}} \frac{\pi}{3} r_c^3 [1-\cos(\theta_{ci})]^2[2+\cos(\theta_{ci})], \tag{24}$$

$$V_{bi} = \frac{\pi}{3} r_{bi}^3 [1-\cos(\theta_{bi})]^2[2+\cos(\theta_{bi})], \tag{25}$$

$$r_c \sin(\theta_{ci}) = r_{bi}\sin(\theta_{bi}), \quad \forall i \in \mathbb{A}, \tag{26}$$

$$\frac{2}{r_c}A(1+\mu)\left[\left(\frac{r_c}{\rho_c}\right)^2 - 1\right] + C\kappa(r_c-\rho_c) = \frac{2}{r_{bi}}A(1+\mu)\left[\left(\frac{r_{bi}}{\rho_{bi}}\right)^2 - 1\right], \quad \forall i \in \mathbb{A}. \tag{27}$$

Equation (23) defines the volume constraint as given by components in Eqs. (24) and (25). Thus, all of the volume contained in the cell body, V_c, and blebs, V_{bi}, add up to the initial value.

Equation (26) consists of $N = |\mathbb{A}|$ equations, as it enforces continuity of the membrane between the cell and each bleb. Similarly, Eq. (27) defines N equations that arise from combining Eqs. (16), (18), and (19) under the assumption that pressure is continuous throughout the cell and blebs, and that there is no cortex to adhere to in the bleb.

Through defining Eqs. (23)–(25), we made the assumption that each bleb only interacts through continuity of pressure and volume. However, when blebs form in direct contact with one another, their interaction will be more complex. We justify our assumption of bleb independence by noting that blebbing is known as a very localized action in that blebs are usually isolated from one another, at least in the satellite stem cells, which we are modeling. Further, it is known that blebs have a small inhibitory effect locally in both space and time [12], that is, if a bleb occurs in a specific location, then another bleb will not appear near the original location for a short time. Both of these characteristics suggest that blebs tend not to have a large effect on one another. By appealing to this assumption, we specify the location of bleb i, through the spherical coordinates (ϕ_i, ψ_i), where the longitudinal and azimuthal angles are chosen uniformly at random from the intervals $[-\pi/2, \pi/2]$ and $[-\pi, \pi)$, respectively.

Equations (23)–(27) represent $2N+1$ constraints on the blebbing cell, i.e., 1 volume constraint, N continuity constraints, and N force balances. However, as noted above, for a cell with N blebs, we need to specify $4N+1$ variables, i.e., 1 cell radius, r_c; N bleb radii, r_{bi}; N bleb reference radii, ρ_{bi}; N neck angles for the bleb, θ_{bi}; and N neck angles for the cell, θ_{ci}; hence, we need to prescribe $2N$ constitutive equations. N constitutive equations are used to specify the region over which the membrane delaminates from the cortex. That is, we fix $\theta_{ci} = \theta_c$ for all blebs. Although, this appears to be a strong assumption, we aim to give an estimate of θ_c, which depends on experimental data, and, so, this can be interpreted as being a mean value of the neck size, which will provide an *a posteriori* check for the validity of this assumption. It should be noted, however, that the bleb neck is actually dynamic as it tears away from the cortex. Since we are using an adiabatic approximation, this simply means that θ_c is the final stabilized value of the variable. Although θ_c is currently undetermined future work will look into the influence of stochastic variation and, perhaps, coupling the neck angle to other cellular processes.

Presently, $3N+1$ degrees of freedom are completely specified. The remaining N degrees of freedom are currently

left free. Either they can be used to define a constitutive evolution equation that models the growth of the reference configuration [32], or, as we will see in Sec. II B, we specify a new geometric relation that links the size of the cell and bleb through their interaction with a substrate.

Consistent with (i) treating θ_c as a fixed control parameter, which will be used in relating the model to experiment; and (ii) blebs not influencing one another; we make a final simplification of dealing with only a single bleb expanding and contracting at a time. As discussed in the introduction we consider a parsimonious model of blebbing, stripped down to its simplest parts. However, the insights will be of use, since once we understand how the system acts with one bleb, generalizing the model will not be difficult.

We are able to generate the maximum bleb size, as limited by the equilibration of the pressure, $\Delta P = 0$. In this case, Eq. (27) is set to zero and, by definition, the cell and bleb radii collapse onto those of their respective reference configurations. Since ρ_c and θ_c are inputs that are constant we can calculate the maximum radius of the bleb, R_b, through the volume constraint,

$$V = V_c + \tfrac{1}{3}\pi R_b^3[1-\cos(\theta_b)]^2[2+\cos(\theta_b)], \tag{28}$$

where $V = (4/3)\pi r_0^3$ and $V_c = (\pi/3)\rho_c^3[1+\cos(\theta_c)]^2[2-\cos(\theta_c)]$. Upon rearranging Eq. (28) and using Eq. (26), we find that R_b satisfies the equation

$$0 = 4(V-V_c)R_b^3 - \pi R_b^2[\rho_c \sin(\theta_c)]^4 - \frac{1}{3}\pi[\rho_c \sin(\theta_c)]^6 - 3\frac{(V-V_c)^2}{\pi}. \tag{29}$$

The accompanying maximum neck angle for the bleb, $\theta_b^{\max}$, can then be found using Eq. (26); however, care needs to be taken due to the nonuniqueness of $\sin(\theta_b)$ for $\theta_b \in [0,\pi]$. Hence, using Eqs. (26) and (28), we derive the following equation in terms of $\cos(\theta_b)$, which is uniquely defined in the given interval,

$$(\Delta V^2+1)\cos\left(\theta_b^{\max}\right)^3 + 3(\Delta V^2+1)\cos\left(\theta_b^{\max}\right)^2 + 3\Delta V^2\cos\left(\theta_b^{\max}\right) + (\Delta V^2-4) = 0, \tag{30}$$

where

$$\Delta V = 3\frac{V-V_c}{\pi\rho_c^3\sin(\theta_c)^3}. \tag{31}$$

Since the equations for R_b and $\cos(\theta_b^{\max})$ are cubic polynomials, they can be solved explicitly. Unfortunately, the analytic solutions are rather cumbersome and offer no real insight into the dependence of R_b or $\theta_b^{\max}$ on the various different parameters, thus we state the full cubic equation instead, with the understanding that it can be trivially solved numerically, or analytically, if needed. Finally, note that the discriminant of Eqs. (29) and (30) can easily be checked, and in both cases they are negative, meaning that the cubic equations have unique real solutions, hence, we do not need to worry about choosing the correct root

B. Adhesion model

We now present a model of adhesion. Evolving adhesions lead to a temporal asymmetry, allowing the cell to move as the blebs cyclically expand and contract. Here, the adhesions are treated as simple springs that break when stretched too far. Critically, we do not consider the actual kinetics of the adhesion binding and unbinding process [37–39]. Not only is this assumption used to retain simplicity in the model, but the adhesion kinetics will only influence the time scale of the process. Since we consider the blebbing "event" (initiation-expansion-adhesion-retraction) as one time unit, this influence on time scale should not change the qualitative results of the paper. We begin by treating the case when the cell is able to adhere to a flat two-dimensional surface.

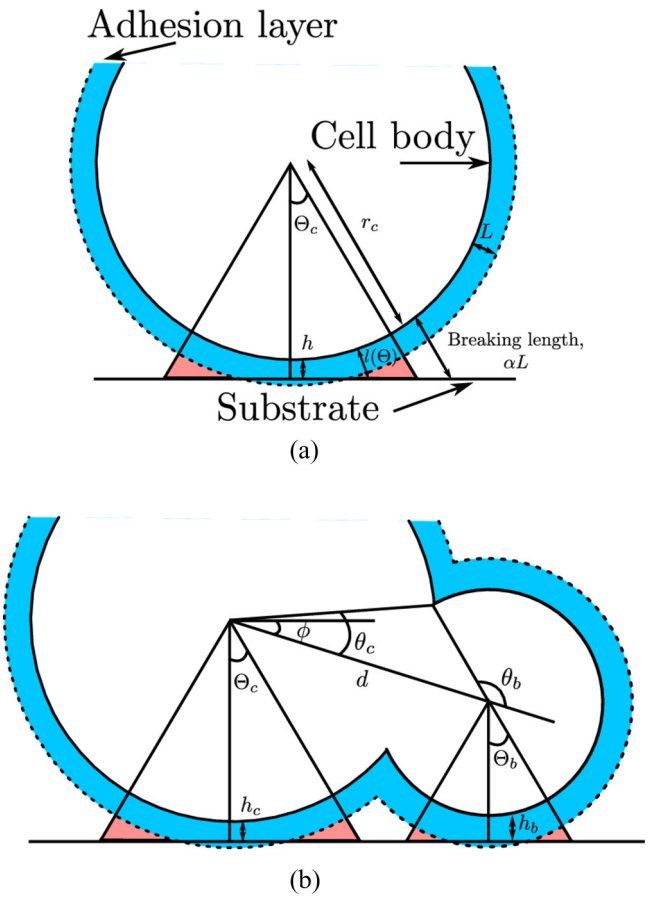

FIG. 4. Schematic diagram of adhesions acting between a substrate and (a) a cell or (b) a cell and a bleb. Variable definitions: (r_c,θ_c), cell radius and neck angle; (r_b,θ_b), bleb radius and neck angle; L, width of resting adhesion layer; αL, maximum width of adhesion layer; Θ_c, half angle subtended by the cell's adhesion pad; Θ_b, half angle subtended by the bleb's adhesion pad; h_c, separation distance of bleb and substrate; h_b, separation distance of cell and substrate; d, distance between cell and bleb centers.

To define the adhesions we prescribe a set of spherical caps concentric around the blebbing cell. This concentric layer represents the resting size, $L \ll r_b$, of the adhesive layer, where L is a new independent parameter [see Fig. 4(a)]. The adhesions are modeled as piecewise Hookean springs that break if extended beyond a critical length, αL, where α is defined as the ratio of resting adhesion length to breaking adhesion length. Further, because the adhesion kinetics of binding and unbinding occur on a fast molecular time scale,

we assume that the system is in mechanical equilibrium at each time point. At equilibrium, the surface and cell are separated by a distance h. The problem is then to resolve forces and torques to find the resting position of the cell and blebs. Initially, we consider a spherical cell body without a bleb, as we will see it generalizes to the single bleb case.

The adhesions are assumed to act normally to the cell surface. This is justified because the adhesions are small, $h < L \ll r_b \leqslant r_c$, and, so, the influence of any perturbations to the orientation will be much smaller. For a single sphere in equilibrium with the substrate, the adhesion pad is symmetric about the lowest point of the cell. Due to this symmetry torque and horizontal force balances are automatically satisfied, leaving us to find the angle Θ_c over which the adhesions bind to the surface, such that the vertical force balance is satisfied [see Fig. 4(a)]. Due to the spherical symmetry of the cell, we only need to consider a one-dimensional slice of the sphere and, further, due to the symmetry about the lowest point, we only need consider the adhesions over a nonnegative range of Θ. Using Fig. 4 and defining h to be the cell-substrate separation distance we derive the equation $l(\Theta)\cos(\Theta) = h + r_c[1 - \cos(\Theta)]$. Thus, neglecting effects of gravity due to the trivial mass of the cell, the vertical force balance is

$$0 = \int_0^{\Theta_c} [L - l(\Theta)]\cos(\Theta) d\Theta, \tag{32}$$

$$= \int_0^{\Theta_c} (L + r_c)\cos(\Theta) - (h + r_c) d\Theta, \tag{33}$$

$$= (L + r_c)\sin(\Theta_c) - (h + r_c)\Theta_c. \tag{34}$$

By geometry, when $\Theta = \Theta_c$,

$$h + r_c = (\alpha L + r_c)\cos(\Theta_c), \tag{35}$$

which, together with Eq. (34), implies

$$\frac{\alpha L + r_c}{L + r_c} = \frac{\tan(\Theta_c)}{\Theta_c}. \tag{36}$$

Since $L \ll r_c$, we must have $\Theta_c \ll 1$, and by linearizing both sides of Eq. (36), we derive the following general approximation:

$$\Theta_c \approx \sqrt{\frac{3(\alpha - 1)L}{r_c}}. \tag{37}$$

Note that $\Theta_c = 0$ is also a solution, which corresponds to the cell lying on top of the substrate without the adhesive layer deforming. However, by comparing the cell-substrate adhesion energy of these two solutions, we verify that Eq. (37) gives the minimum energy solution.

Substituting Eq. (37) into Eq. (35), we find that

$$h \approx \frac{(3 - \alpha)L}{2}. \tag{38}$$

Equations (37) and (38) are simple estimates that predict how the cell will behave upon perturbing the parameters. In particular, since the adhered surface area is proportional to $r_c^2\Theta_c$, Eq. (37) predicts that the adhered surface area will scale as $r_c^{3/2}$. Similarly, we find that to satisfy the condition that the cell does not penetrate the substrate, $h \geqslant 0$, we must have $\alpha < 3$. This provides a natural limit for how far the adhesions can stretch for a spherical cap model, namely, they can extend, at most, three times their natural length, which is consistent with experiments [35].

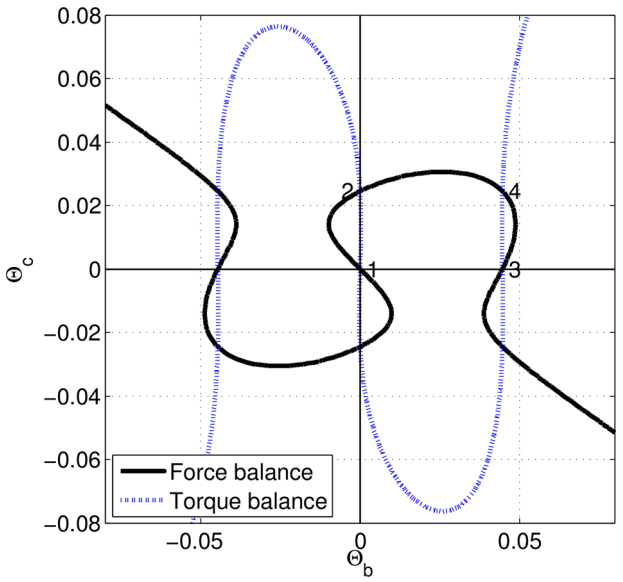

FIG. 5. Roots of the force and torque balance equations. The points 1–4 are the values of Θ_b and Θ_c that simultaneously solve both equilibrium functions. Although we are specifically interested in the nonnegative quarter plane, the whole plane is shown to illustrate the rotational symmetry that is present in the solutions. Parameters are $r_c = 5\,\mu$m, $r_b = 1.5\,\mu$m, $\theta_c = 1/5$, $L = 10^{-3}\,\mu$m, $\alpha = 2$, and θ_b is found through Eq. (26).

We extend this analysis to a cell and bleb configuration. First, we show that the torque balance is automatically satisfied and, thus, all of the derivations presented above for the single sphere can be generalized to the cell and single bleb case.

An intuitive argument proceeds as follows: suppose that the cell and bleb as a system is in equilibrium both in terms of its forces and torques. Further, suppose they are not independently in force equilibrium. Due to the quick relaxation speed of the molecular kinetics, and the fact that the adhesion pads for the cell and bleb do not interact, then the adhesion pads will be symmetric about the lowest points of the cell and bleb, respectively. Thus, horizontal forces must balance, meaning that only vertical forces are not in equilibrium. Suppose, without loss of generality, that the cell experiences a net upwards force, implying that, since the whole cell-bleb system is in equilibrium, the bleb must experience a net downwards force. However, this causes a nonzero torque to exist about the center of mass. Hence, we produce a contradiction demonstrating that the cell and bleb must be in equilibrium separately.

To illustrate this property here, we have plotted the locus of the roots for the total force and torque balances in Fig. 5 [equations not shown, but they can be derived in a similar manner to Eqs. (32)–(34)]. The functions only share four roots in the nonnegative quarter plane, denoted 1–4, and represent the roots $(0,0)$, $(0,\Theta_{0c})$, $(\Theta_{0b},0)$, and $(\Theta_{0b},\Theta_{0c})$, respectively, where Θ_{0c} is given by Eq. (37) and Θ_{0b} is given by Eq. (37) with r_c changed to r_b. Of these four solutions $(\Theta_{0b},\Theta_{0c})$ has the lowest energy.

Second, we compute the maximal radius taking into account that an expanding bleb will stop growing when it hits the substrate, which can happen before it has reached the global maximum radius derived from Eq. (29). The bleb may, or may not, interact with the substrate depending on the angle, ϕ, at which the bleb is initiated as seen in Fig. 4(b). In general, we have

$$d = r_c \cos(\theta_c) - r_b \cos(\theta_b), \tag{39}$$

and that the global maximum bleb radius, $r_b = R_b$, occurs when $r_c = \rho_c$. From these values, we know that the bleb will touch the substrate whenever $\phi \in [-\pi/2 + \Theta_c + \theta_c, \Phi]$, where

$$\sin(\Phi) = \frac{(R_b + \alpha L)\cos(\Theta_b) - (\rho_c + \alpha L)\cos(\Theta_c)}{\rho_c \cos(\theta_c) - R_b \cos\left(\theta_b^{\max}\right)}. \tag{40}$$

Thus, Φ is defined to be the maximum angle that an expanded bleb can touch the substrate.

In the region $[-\pi/2, -\pi/2 + \Theta_c + \theta_c]$ the cell is already touching the substrate through the adhesions and, so, no bleb expands. We use the dependence of Θ_c and Θ_b on L and $L \ll r_b \leqslant r_c$ to expand Eq. (40) with respect to L/r_b to obtain

$$\sin(\Phi) = \frac{R_b - \rho_c}{\rho_c \cos(\theta_c) - R_b \cos(\theta_b^{\max})} + \mathcal{O}[(L/r_b)^2]. \tag{41}$$

In the complementary region, $[-\pi/2 + \Theta_c + \theta_c, \Phi]$, we define a function for the maximum radius of the bleb, $r_b^{\max}$, by expanding the geometric constraint,

$$(r_c + \alpha L)\cos(\Theta_c) + d\sin(\phi) = (r_b + \alpha L)\cos(\Theta_b), \tag{42}$$

to obtain

$$r_c + d\sin(\phi) = r_b + \mathcal{O}(L/r_b). \tag{43}$$

Combining Eqs. (26) and (43), we obtain the approximate relationships

$$r_b^{\max} \approx r_c\left[2\frac{1 + \sin(\phi)\cos(\theta_c)}{\cos(\phi)^2} - 1\right], \tag{44}$$

with corresponding angle given by

$$\cos(\theta_b) = \frac{-2\sin(\phi)\sin(\theta_c)^2}{\sin(\phi)^2 + 2\sin(\phi)\cos(\theta_c) + 1} - \cos(\theta_c). \tag{45}$$

In deriving Eqs. (44) and (45), we neglected the trivial root $r_c = r_b$ and $\theta_c = \theta_b$, which corresponds to the unblebbed case. It can be seen that since $\theta_c > 0$ and $\pi/2 > \Phi > -\pi/2$, then both $r_b^{\max}$ and θ_b are well-defined in terms of their existence and uniqueness.

Finally, Eqs. (44) and (45) can be combined with the volume Eqs. (23)–(25) to give

$$r_c^3 = \frac{3V\left\{3\frac{[2+\cos(\theta_c)-\sin(\phi)]}{1+\cos(\theta_c)}\cos(\phi)^4 - 4[3 - 2\sin(\phi)]\cos(\phi)^2 + 8[1 - \sin(\phi)]\right\}}{2\pi[1 + \cos(\theta_c)]^3\left\{\frac{9\cos(\phi)^4}{1+\cos(\theta_c)} + 3[3\cos(\theta_c) - 7]\cos(\phi)^2 - 8[\cos(\theta_c) - 2]\right\}}, \tag{46}$$

which depends solely on θ_c, a constant, and ϕ, a uniform random variable. We are interested in using θ_c as a control parameter for the system as it is an experimentally measurable quantity, which can be linked to the motility characteristics of the cells.

The assumption that the bleb stops growing once it hits the substrate can easily be relaxed. Specifically, we would assume that as the bleb continues to grow, the cell would not be moved as it is more adhered to the substrate than the growing bleb. If the bleb did move the cell while it was growing, then it would result in the cell moving in the opposite way to bleb expansion, which is not experimentally observed. Hence, at most, the cell would rotate to accommodate the growing bleb. Since, in the case of muscle stem cells, the expansion phase does not result in translation of the cell, then altering how the bleb grows in relation to the substrate would simply result in changing the probability density function of bleb sizes, which is easily incorporated in Sec. II C. However, for clarity, we persist with the idea that the bleb stops growing upon contact with the substrate.

In Fig. 6, we illustrate the model from Secs. II A and II B. The configurations are produced under the assumption that the bleb's size is limited either by its interaction with the substrate or the conservation of the total cell volume, which is constrained under the assumption that $\Delta P = 0$ at equilibrium.

The small size of the adhesions that stick the cell and bleb to the substrate has a number of implications. First, the three concentric shells, which represent the membrane; resting adhesion length and maximally stretched adhesion length, respectively, look as though they rest on top of one another. However, a magnified version of the adhesion pad, in the top left inset of Fig. 6, demonstrates that these three shells are separate. Second, the size of the adhesion pad depends on the angular region over which the stretched adhesion touch the substrate, i.e., the width of the adhesion pad is $2r_c\sin(\Theta_c) = \sqrt{3r_c(\alpha - 1)L}$. In the limit $L \to 0$, we could forego adhesion considerations altogether and simply assume that cell and blebs rest fully on the substrate, indicating that adhesions only occur at the point of touch between the substrate and the sphere. However, the scales derived above relating the size of the sphere and its adhesion pad as well as the restriction on the parameter α more than justify the inclusion of adhesion considerations.

The other two-dimensional plots in Fig. 6 demonstrate the ability of the cell to bleb over its entire body (save a small area over which the cell is adhered to the substrate). Moreover, in the bottom left and right plots of Fig. 6, we see the influence of the substrate on the expansion of a bleb. By comparing the lengths of the thick black lines, connecting the center of the cell to the center of the bleb, we see that the maximally extended bleb (bottom left of Fig. 6) is configured in such a way that its center is outside of the cell's body, whereas the bleb that was initiated at an angle closer to $-\pi/2$ (bottom right of Fig. 6) is unable to extend as far, and its center is still inside the cell's body.

The plots of Fig. 6 were all numerically obtained from the exact, nonlinear forms of the relations between the variables.

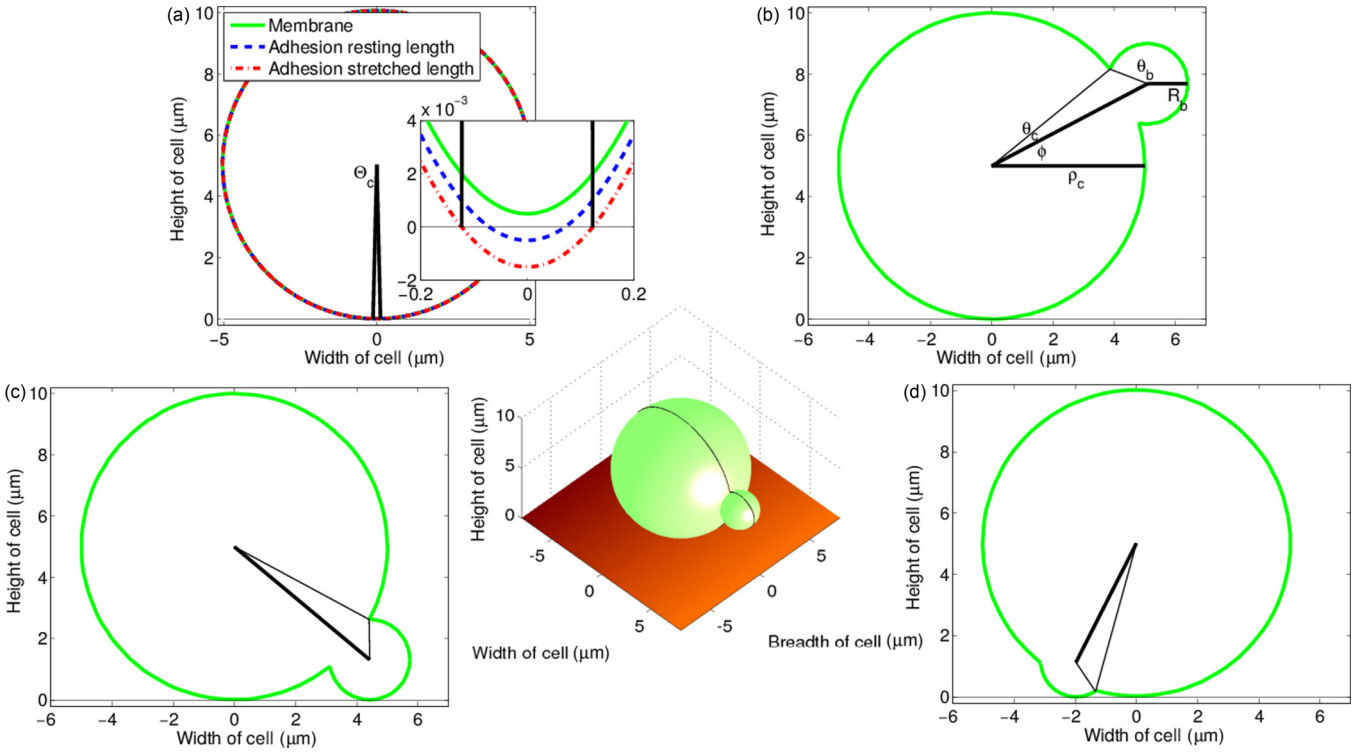

FIG. 6. A blebbing cell, adhering to a flat substrate. In all cases the full nonlinear system, Eqs. (23)–(27), (36), and (40), were solved numerically using a Newton-Raphson iteration scheme. The center shows a fully rendered three-dimensional cell adhered to a two-dimensional flat substrate, with a bleb extended to its maximum distance. The black line along the three-dimensional body illustrates the plane of symmetry normal to the substrate. The surrounding images are cross sections of a blebbing cell. (a) Initial spherical cell adhered to the substrate, which also illustrates the concentric shells of the adhesions at their resting length and full extended length. The inset illustrates a magnified section of the adhesion pad. The black solid lines illustrate size of the adhesion pad, which depends on Θ_c. (b) A cell with a bleb that was initiated at an angle $\phi > 0$, which will never touch the substrate and, thus, extends to its maximum size. The variables ϕ, ρ_c, θ_c, R_b, and θ_b are also presented in the image. (c) A bleb is extended at an angle $\phi = \Phi$, hence, the bleb is just touching the substrate and, so, the bleb is able once again to extend to its maximum size. (d) A bleb for which $\phi \in [-\pi/2 + \Theta_c + \theta_c, \Phi]$ and, thus, it is unable to grow to its maximum size, before it interacts with the substrate. Parameters are $\rho_c = 5\,\mu$m, $\theta_c = 1/5$, $L = 10^{-3}\,\mu$m, $\alpha = 2$, $\kappa C = 1000\,\text{pN}/\mu\text{m}^3$, $A = 400\,\text{pN}/\mu$m, $\mu = 0.5$ and, initially, $\Delta P = 40\,\text{pN}/\mu\text{m}^2$.

In Fig. 7, we compare these numerical solutions with their linear approximation. We note that it is only within the adhesion pad region, $\phi \in [-\pi/2, -\pi/2 + \Theta_c + \theta_c]$, that the approximation breaks down. This discrepancy is expected because the adhesion pad region is assumed to inhibit blebbing, thus, within this region there should be no blebbing. Indeed, the numerical approximations reproduce this solution as they are fixed to the initial radius constant, R_0, within the adhesion pad region. Whereas in the adhesion pad the linear approximation slightly overestimates r_c, the estimates for r_b become increasingly disparate as $\phi \to -\pi/2$ because of the singularity in Eq. (44), which specifies r_b.

C. Stochastic blebbing

Since the adhesion pad of a spherical cap scale as $r^{3/2}$, the cell's adhesion pad will be larger than a bleb's adhesion pad. Thus, as a bleb retracts the cell adheres more to the surface than the bleb and, hence, the retraction preferentially causes the bleb's adhesion to break. Without taking into account other processes, this motion results in a time reversal of the expansion process. To break this symmetry, we assume that adhesions weaken over time. Thus, the blebbing process proceeds as follows:

(1) Initially, a spherical cell adheres to the substrate.

(2) Initiate bleb expansion somewhere on the cell surface by randomly sampling (ϕ, ψ). Compute R_b from Eq. (29).

(3) Depending on (ϕ, ψ) and R_b, calculate whether the bleb will intersect with the substrate or not.

(4) Expand the bleb to its maximum size, which will be $r_b^{\max}$ [computed from Eq. (44)] or R_b, depending on stage 3.

(5) Fix adhesions to the bleb while weakening adhesions that couple cell and substrate.

(6) Retract the bleb into the cell, allowing the cell's position to update to that of the bleb.

This process captures the main qualitative features of the bleb dynamics over the time scale of its cycle (2–3 mins) and represents one discrete event that we can iterate in time. The motion of the cells is driven by the size and displacement of the blebs. In this section, we consider the stochastic production of these blebs and use it to derive rates of random motion. Further, depending on the results of Sec. II B, we take the limit of $L \to 0$ (and, thus, $\Theta_c \to 0$) and fix r_c to be constant.

As illustrated in Figs. 3 and 4, the two angles that are controlled stochastically are $\phi \in (-\pi/2, \pi/2]$, representing

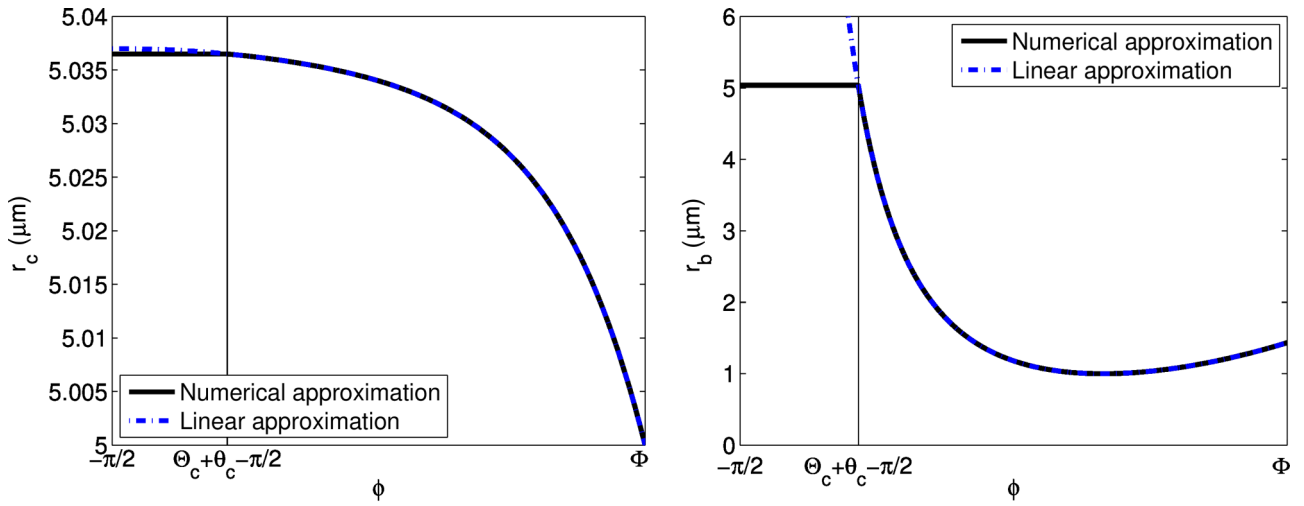

FIG. 7. Comparing numerical and linearized approximate solutions for (a) r_c and (b) r_b within the region $\phi \in [-\pi/2, \Phi]$. Parameters are the same as described in the caption of Fig. 6.

the altitude angle of the bleb, and $\psi \in [0, 2\pi]$ representing the azimuthal angle of the bleb. Thus, ϕ determines whether the bleb hits the substrate, whilst ψ determines the direction of movement. Initially, we assume the angles are uniformly distributed in their respective intervals and look for the probability density function of cell movement distance.

For a given angle, $\phi \in [-\pi/2 + \theta_c, \Phi]$, a single expansion and contraction will cause the cell center to move a distance of $w = d\cos(\phi)$. Using the continuity equations, Eqs. (39) and (42), the equation for w becomes

$$w = \begin{cases} \frac{2r_c}{\cos(\phi)}[\sin(\phi) + \cos(\theta_c)] & \phi \in [-\pi/2 + \theta_c, \Phi], \\ 0 & \text{otherwise.} \end{cases} \tag{47}$$

We define the largest distance that the cell center can move to be

$$\hat{w} = \frac{2r_c}{\cos(\Phi)}[\sin(\Phi) + \cos(\theta_c)], \tag{48}$$

which occurs when $\phi = \Phi$. Further, we define $f(w)$ to be the probability density function, which describes the relative likelihood for the random variable, W to take a given value, w, which depends on the uniformly random variable ϕ. The probability of W falling within a particular interval is given by the integral of f over that interval. To calculate $f(w)$, we first consider the cumulative distribution, $F(w)$, which describes the probability that W will value less than or equal to w. Specifically,

$$F(w) = P(W \leqslant w) \quad \text{for } w \in [0, \hat{w}], \tag{49}$$

$$= P(W = 0) + P\left\{\frac{2r_c}{\cos(\phi)}[\sin(\phi) + \cos(\theta_c)] \leqslant w\right\}, \tag{50}$$

$$= P(W = 0) + P\left\{\phi \leqslant \arctan\left(\frac{w}{2r_c}\right) - \arcsin\left[\frac{2r_c}{\sqrt{w^2 + 4r_c^2}}\cos(\theta_c)\right]\right\}, \tag{51}$$

$$= P(W = 0) + \int_{\theta_c - \pi/2}^{\arctan(w/2r_c) - \arcsin[2r_c\cos(\theta_c)/\sqrt{w^2+4r_c^2}]} \frac{1}{\pi} d\phi, \tag{52}$$

where we have inverted the formula for w in Eq. (51) and used the definition of the uniformly random distribution, ϕ, in Eq. (52). From Eq. (47), we have

$$P(W = 0) = \frac{\pi/2 + \theta_c - \Phi}{\pi}, \tag{53}$$

which gives

$$F(w) = \begin{cases} 0 & w < 0, \\ \frac{\pi - \Phi}{\pi} + \frac{1}{\pi}\left[\arctan\left(\frac{w}{2r_c}\right) - \arcsin\left(\frac{2r_c\cos(\theta_c)}{\sqrt{w^2+4r_c^2}}\right)\right] & 0 \leqslant w \leqslant \hat{w}, \\ 1 & \hat{w} < w. \end{cases} \tag{54}$$

Note that by using the definition of $w(\phi)$ and its inverse, we see that $w = \hat{w}$ when $\phi = \Phi$; i.e.,

$$\Phi = \arctan\left(\frac{\hat{w}}{2r_c}\right) - \arcsin\left(\frac{2r_c\cos(\theta_c)}{\sqrt{\hat{w}^2+4r_c^2}}\right). \tag{55}$$

Hence, $F(\hat{w}) = 1$, which further implies that $P(W = 0) < 1$.

By definition, the cumulative distribution is related to the probability density function through the identity

$$f(w) = \frac{dF(w)}{dw}. \tag{56}$$

Specifically, for $0 \leqslant w \leqslant \hat{w}$,

$$f(w) = \frac{\pi/2 + \theta_c - \Phi}{\pi}\delta(w) + \frac{2r_c}{4r_c^2 + w^2}\left[1 + \frac{w\cos(\theta_c)}{\sqrt{w^2 + 4r_c^2\sin(\theta_c)^2}}\right], \tag{57}$$

where $\delta(w)$ is the standard Dirac δ function. The first and second moments can then be directly calculated and compared to available data. These moments are given here, as they will be of use later on:

$$\begin{aligned}\langle W\rangle = \frac{\hat{w}\Phi}{\pi} - \frac{1}{\pi}\Bigg\{&\hat{w}\arctan\left(\frac{\hat{w}}{2r_c}\right) + r_c\ln\left(\frac{4r_c^2}{\hat{w}^2+4r_c^2}\right) + 2\cos(\theta_c)r_c\ln\left[\frac{2r_c\sin(\theta_c)}{\sqrt{\hat{w}^2+4r_c^2\sin(\theta_c)^2}+\hat{w}}\right]\\ &+ 2r_c\,\mathrm{arctanh}\left[\frac{\hat{w}\cos(\theta_c)}{\sqrt{\hat{w}^2+4r_c^2\sin(\theta_c)^2}}\right] - \hat{w}\arcsin\left[\frac{2r_c\cos(\theta_c)}{\sqrt{\hat{w}^2+4r_c^2}}\right]\Bigg\},\end{aligned} \tag{58}$$

$$\begin{aligned}\langle W^2\rangle = \frac{\hat{w}^2\Phi}{\pi} + \frac{1}{\pi}\left(4r_c^2+\hat{w}^2\right)\left\{\arcsin\left[\frac{2r_c\cos(\theta_c)}{\sqrt{\hat{w}^2+4r_c^2}}\right] - \arctan\left(\frac{\hat{w}}{2r_c}\right)\right\}\\ - \frac{2r_c^2}{\pi}[\sin(2\theta_c) + \pi - 2\theta_c] + \frac{2r_c}{\pi}\left[\cos(\theta_c)\sqrt{\hat{w}^2+4r_c^2\sin(\theta_c)^2} + \hat{w}\right].\end{aligned} \tag{59}$$

Although we have constructed the probability density function for the distance moved by the cell during each bleb cycle, experimentalists do not have direct access to this data. Instead, data is often in the form of time-evolving trajectories that have been tracked over the course of an experiment. Thus, we extend the analysis assuming that individual bleb steps are independent and identically distributed. Explicitly, if $P(\boldsymbol{x},n)$ is the probability density function for the displacement of the cell on the nth step, the evolution of this position is governed by the general equation [40]

$$P(\boldsymbol{x},n+1) = \int P(\boldsymbol{x}-\boldsymbol{s},n)p(\boldsymbol{s})d\boldsymbol{s}, \tag{60}$$

where $p(\boldsymbol{s})$ is the probability density function for a movement from the origin to a point $\boldsymbol{s} = [w\cos(\phi), w\sin(\phi)]$, that is $p(\boldsymbol{s}) = f(w)/2\pi$. Using the probability distribution, we are able to compute the expected value of any functional form of the variables, $g(\boldsymbol{X})$, over a number of blebbing events through

$$\mathbb{E}_n[g(\boldsymbol{X})] = \int g(\boldsymbol{x})P(\boldsymbol{x},n)d\boldsymbol{x}. \tag{61}$$

In particular, we are interested in the moments of the distribution.

First, we note that since the random walk of the cells is symmetric then the average position of all the cells is the initial origin, i.e., $\mathbb{E}_n(X) = \mathbb{E}_n(Y) = 0$ for all n. Further, we are particularly interested in the second moments of the probability density as they are often used to characterize specific motion patterns as they can be compared with the mean-squared displacement of the experimental trajectory data. Higher-order moments can be calculated using the characteristic function as derived in the Appendix.

Since each blebbing event is independent and identically distributed, the variance of the cell's position is simply the sum of the step-size variances:

$$\mathbb{E}_n(X^2 + Y^2) = n\langle W^2\rangle. \tag{62}$$

This property suggests that we can approximate the position distribution of the cells as a multivariate Gaussian distribution,

$$g(x,y,t) = \frac{1}{2\pi\nu^2 t}\exp\left[\frac{-1}{2\nu^2 t}(x^2+y^2)\right], \tag{63}$$

with variance, $\nu^2 = \langle W^2\rangle/2$. Further, we can rely on the central limit theorem, which will cause $P(\boldsymbol{x},n)$ to converge to a Gaussian as n increases. Note that since the blebbing motion we are investigating is a random walk with variable step length, then this approximation should be accurate everywhere, except near the origin. The origin will be problematic for this continuous approximation, because of the δ function in Eq. (57).

III. RESULTS

In this section, we compare the approximations derived in Sec. II with the distributions extracted from stochastically simulated populations of blebbing cells, to link experimental data to the properties of the cell.

A. No volume constraint

Initially, we do not constrain the volume. Instead, we use this degree of freedom to fix Φ [as defined by Eq. (40)] to specific values to obtain the relationship between the critical

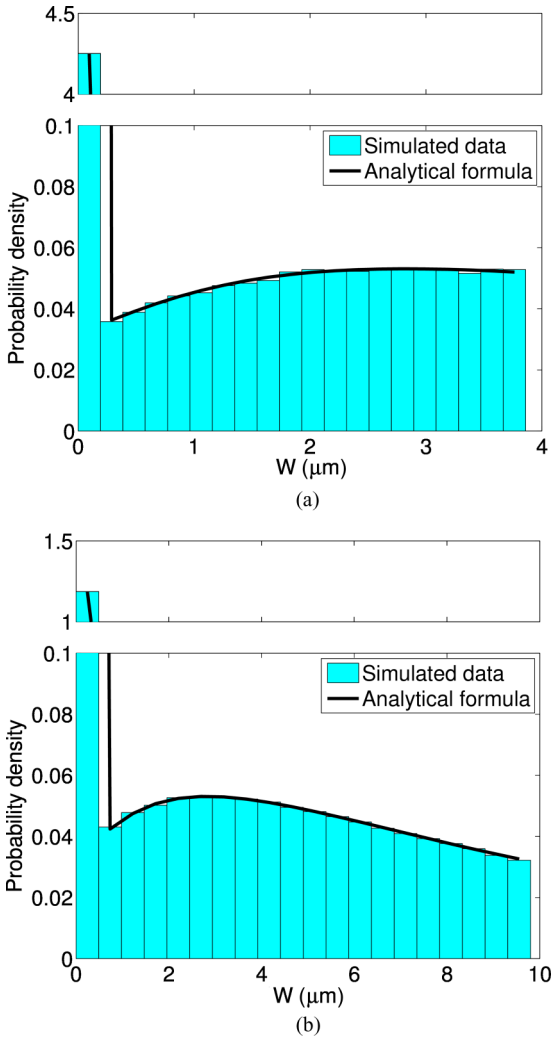

FIG. 8. Comparison of the probability density function for the random variable W calculated approximately from 10^5 observations of a simulated blebbing cell (shown as a histogram) and directly, through Eq. (57). The parameter values are $r_c = 5\,\mu$m, $\theta_c = 1/5$, (a) $\Phi = -\pi/4$ and (b) $\Phi = 0$. Note that the first column of the histogram contains the Dirac δ function contribution.

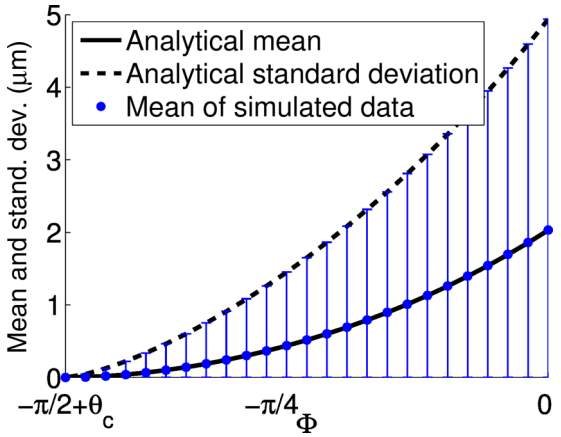

FIG. 9. Comparison of the mean and standard deviation of W as estimated from 10^5 stochastic simulations of a simulated blebbing cell or calculated from Eqs. (58) and (59). The black solid and dashed lines represent analytically derived quantities, while the (blue) points represent the sample mean and the thin (blue) vertical lines represent one standard deviation about the mean. The parameter values are $r_c = 5\,\mu$m and $\theta_c = 1/5$.

blebbing angle and the length of one step, w. By varying Φ we gain insight into the cases where the arrest of bleb growth occurs through the repolymerization of the cortex in the bleb. In this case, the bleb size is not dependent on pressure, and, therefore, volume. Thus, we have more freedom to choose the maximum blebbing angle. The simulations proceed by generating a large number of values of $\phi \in [\theta_c - \pi/2, \Phi]$ and calculating the corresponding values of w, which we can compare the formulas against.

Our first result, presented in Fig. 8, compares the analytically derived probability distribution for the movement distance, Eq. (57), with a normalized histogram, calculated from the observations of W from the stochastic simulations. We observe that the analytical solution compares extremely well with the simulated data, justifying the first-order simplifications of fixing r_c to be constant and $\Theta_c = 0$.

Note that since we are dealing with a continuous probability density function, the probability of any particular given value of observation $0 < w$ is zero and, thus, $P(W = w) = 0$. Instead, a nontrivial range must be provided. The function is then integrated over this given range resulting in a value for the probability that W is within the given range. This difference between probability and probability density becomes important when the probability density function takes values larger than one (note the broken axis of Fig. 8).

The large probability density in the first bar, nearest zero, confirms that three-dimensional blebbing on a two-dimensional substrate is particularly inefficient, as most of the time the cell does not move at all. This inefficiency is due to only a small number of all the blebs actually expanding in the direction of the substrate and, moreover, being able to grow to a size that is able to reach the substrate, thereby causing movement.

By comparing Figs. 8(a) and 8(b), we confirm that as Φ increases, so does the range of W and, in turn, so does the maximum possible value, $\hat{w}$ [see also Fig. 10(a)]. Equally, as Φ increases, more blebs are able to successfully generate movement, causing $P(W = 0)$ to decrease, as it is above four in Fig. 8(a), but only just above one in Fig. 8(b). Furthermore, we notice that the probability densities have an internal local maximum [seen clearly around $W \in [2,4]\,\mu$m in Fig. 8(b)].

By additionally considering Fig. 9 (which again illustrates an excellent comparison between theory and simulated data), we see that despite this lower probability weighting for larger steps, the mean step length and standard deviation increase with Φ. However, the local internal maximum (along with the delta function at $w = 0$) of the probability density means that $\langle W \rangle$ is always much smaller than $\hat{w}$ [see Fig. 10(a)].

The derivative with respect to Φ of the difference $\hat{w} - \langle W \rangle$ is illustrated in Fig. 10(b). This gives us a sense of how these two quantities are related to one another as Φ increases. We note that even though the derivative is always positive and, thus, the two quantities are always diverging away from one another, there is clearly a local minimum in this divergence

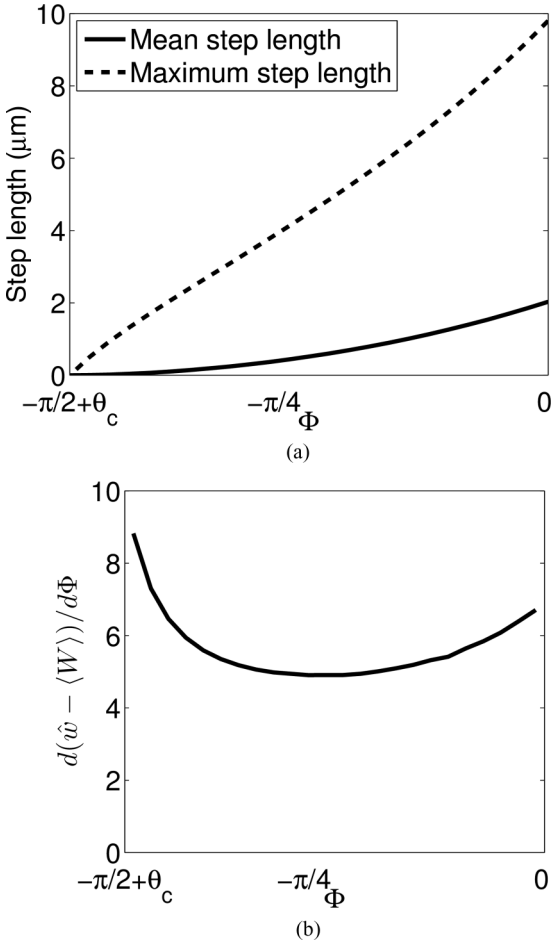

FIG. 10. Visualizing the relationship between the mean and maximum values of W. (a) Comparison of the mean and maximum of W, as Φ is varied, using Eqs. (58) and (48). (b) Divergence rate of the mean and maximum of W, as Φ is varied. The parameter values are the same as in Fig. 9.

rate. Thus, we predict that there is an extremal choice between how far a cell can move on average and how far it can maximally move in one step. Explicitly, if the blebs of the numerical simulation are constrained to be small, then the cell will hardly move during a blebbing event. Conversely, if the blebs in the simulations are allowed to vary over a large range of sizes, then we see that the mean step size does not increase as quickly as the maximum step size, suggesting that these larger blebs occur too infrequently to be significant for motion.

B. Multiple blebbing events

Next, we consider the spatial probability distribution over multiple blebbing events and its approximation to the Gaussian distribution, as derived in Eq. (63) (see Fig. 11).

By comparing Figs. 11(a)–11(d), we see that the cells spread radially about the origin. Moreover, although the Gaussian distribution always underestimates the density near the origin [due to the δ function that occurs in the probability density function, Eq. (57)], we observe that as t increases comparison between the point distribution and the surface given by Eq. (63) improves as a consequence of the central limit theorem.

C. Constrained volume

Finally, we reinstate the volume constraint meaning that upon fixing the cellular structural parameters: ΔP_0, ρ_c, A, $C\kappa$, μ, and θ_c (as defined in Sec. II) the variables: r_c, R_b, $\theta_b^{\max}$, Φ, and $\hat{w}$ are uniquely defined. Knowing these variables allows us to calculate the moments of the random variables W, X, and Y and, hence, the migration properties of our blebbing cell model. Thus, our geometric model links observable migration to unobservable parameters. We choose θ_c as a control parameter since the other variables can be estimated [13,21,35,36,41,42], and because θ_c is a geometric variable related to the width of the bleb neck and, in turn, the region of cortex that becomes delaminated from the membrane during the initiation of a bleb. Thus, it can be calculated from observations, which we consider later.

Due to the volume constraint, as θ_c increases, the neck gets wider and, so, the bleb does not protrude from the cell as far. Namely, we see in Fig. 12(a) that as θ_c is increased from zero, the maximum step length, $\hat{w}$, reduces to zero. Conversely, R_b increases, which may appear counterintuitive. We may think that a bleb with a larger radius would be able to reach further. However, as θ_c increases, the bleb neck becomes wider, causing the curvature of the bleb to become smaller [see Figs. 12(c)–12(e)].

Similar deductions can be made from Fig. 12(b), although the illustrated curves are not monotonic in contrast to Fig. 12(a). Specifically, $\theta_b^{\max}$ initially decreases, demonstrating that the blebbing angle decreases as the bleb is withdrawn into the body [compare Fig. 12(c) and 12(d)]. As θ_c increases further, $\theta_b^{\max}$ reaches a minimum and then increases again. The increase occurs because the neck width is so large that the cell body and bleb spheres essentially collapse onto one another [see Fig. 12(e)], and, hence, $\theta_b^{\max} \approx \theta_c$.

The relationship between Φ [as defined by Eq. (40)] and θ_c is similarly nonmonotonic. However, it is the dependence of the interval $[-\pi/2+\theta_c, \Phi]$ on θ_c that is most significant. Namely, as θ_c increases, the interval rapidly shrinks. Thus, not only do wide blebs have a smaller maximum step distance [see Fig. 12(a)], but equally, the angular range of ϕ over which blebs can be produced, which actually cause movement, is also greatly reduced.

In summary, the mathematical results in the last three paragraphs, pertaining to Fig. 12, can be simplified into the biological result that as the bleb neck size increases the cells will move much slower. This prediction is confirmed in Fig. 13, where we see an extremely rapid drop off of $\langle W^2 \rangle$ as θ_c increases. Indeed, cells that produce blebs with neck angles wider than $\pi/8$ are predicted to be extremely inhibited in their motion. Further, it is consistent with experimental data [13], where it was seen that cells that produce blebs with consistently larger necks produce much slower motion.

We now make use of published data. According to Collins-Hooper *et al.* [13], young satellite muscle stem cells have an average one-dimensional diffusion rate of $D \approx 12\,\mu\text{m}^2/\text{min}$. Moreover, there are on average 30 blebbing events per unit time. Comparing the diffusion rate with the mean-square

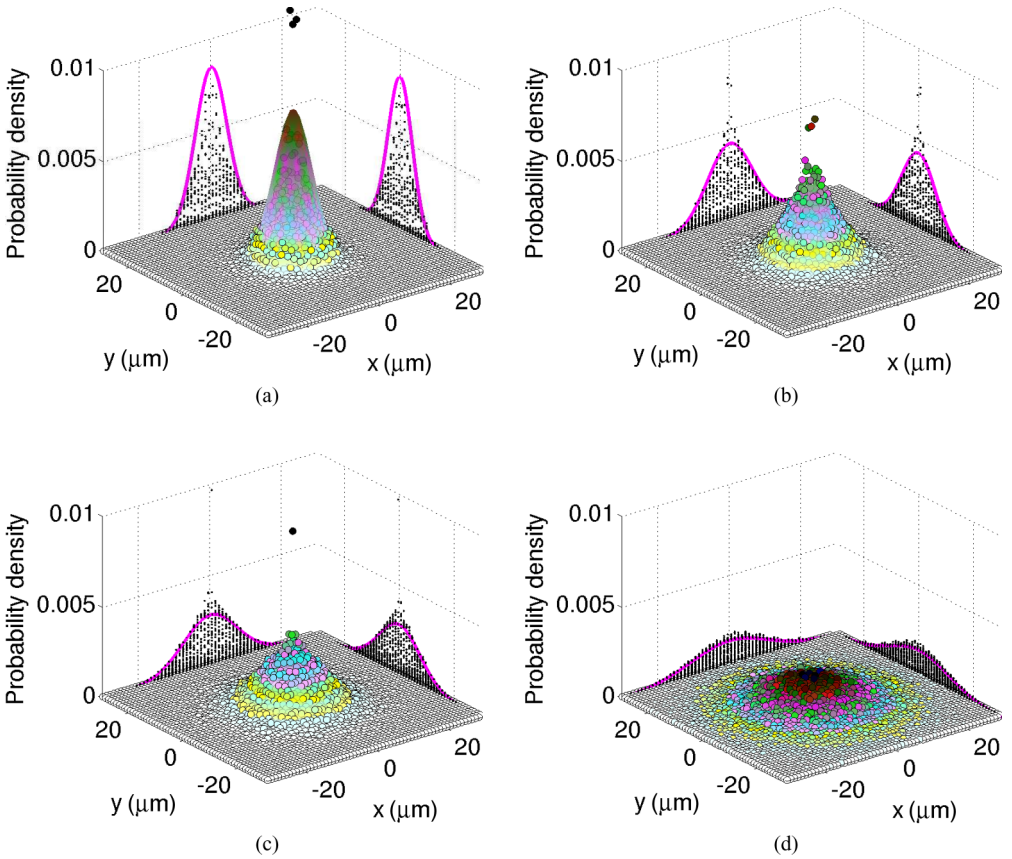

FIG. 11. Comparisons of the probability density functions of a cell being at a position (x, y) over time, where time is measured in terms of the number of blebbing events, (a) $t = 3$ blebbing events; (b) $t = 6$ blebbing events; (c) $t = 9$ blebbing events; (d) $t = 18$ blebbing events. The filled circles illustrate a two-dimensional histogram derived from 10^5 simulations. Each histogram column has a base area of 1 μm^2. The shaded smooth surface is the Gaussian approximation, Eq. (63). To aid visualization, the simulations and approximation have been projected along the x and y directions illustrating the fit. The parameter values are $r_c = 5\,\mu$m, $\theta_c = 1/5$, and $\Phi = -\pi/4$. Note that the z axis has been truncated at 0.01. The coloration of the surface and points is to aid visualization only.

displacement, we have $2D = 24 = 30\nu^2 = 15\langle W^2\rangle$, thus, $\langle W^2\rangle = 1.6\,\mu$m^2. Using a root-finding algorithm on the curve illustrated in Fig. 13, we find that this corresponds to $\theta_c \approx 0.2$, which is within with the range that is observed in the literature and, in particular, corresponds to the neck size seen in Fig. 1. However, it should be noted that, depending on the type of the cell, the age of the cell, and what treatments have been applied to the cell, θ_c can cover a range from 0.05, for very small blebs, to 0.9, for wide blebs that undergo circus motion [12].

IV. SUMMARY AND CONCLUSION

We have derived a simple geometric model of blebbing based on a mechanical model. The simplification was based on the assumption that the cell and blebs maintain spherical symmetry throughout their expansion and retraction phases. Further, by assuming that the blebs were independent, this model produces an active dynamical model of cyclical bleb expansion and contraction. This structure was then placed on a two-dimensional substrate to which it was allowed to adhere.

Assuming that only a single bleb event occurs at any given time, we derived analytical formulas linking the geometry and, most notably, migration properties of the blebbing cell with the fundamental structural parameters of the cell. Critically, we showed that even though the cell may undergo a random walk, with non-Gaussian distributed step sizes its long-time motion is well approximated by a Gaussian function with parameters linked to cell-level properties.

Here, we use a uniform random distribution of bleb locations, suggested from experimental observations. Other cell types may bleb in a polarized manner. This would lead to an alternative distribution of blebs that could be incorporated in the following framework, which is intentionally general. Although the resulting expressions may not be analytically tractable, it should still be possible to numerically simulate the results. These simulations, in turn, will provide insights into how the movement of a cell depends on the underlying blebbing distribution. This work is intended as a future consideration for the authors. Further, the presented model only contains stochastic terms in the location of bleb appearance. However, blebbing cells are known also to contain stochastic neck sizes. Equally, the substrate that the cell moves upon will frequently contain random heterogeneities. It is our intention that the future work will include such probabilistic factors.

We have only chosen to vary θ_c, while fixing the parameters ΔP_0, ρ_c, A, $C\kappa$, and μ. If, instead, we wanted to use the model

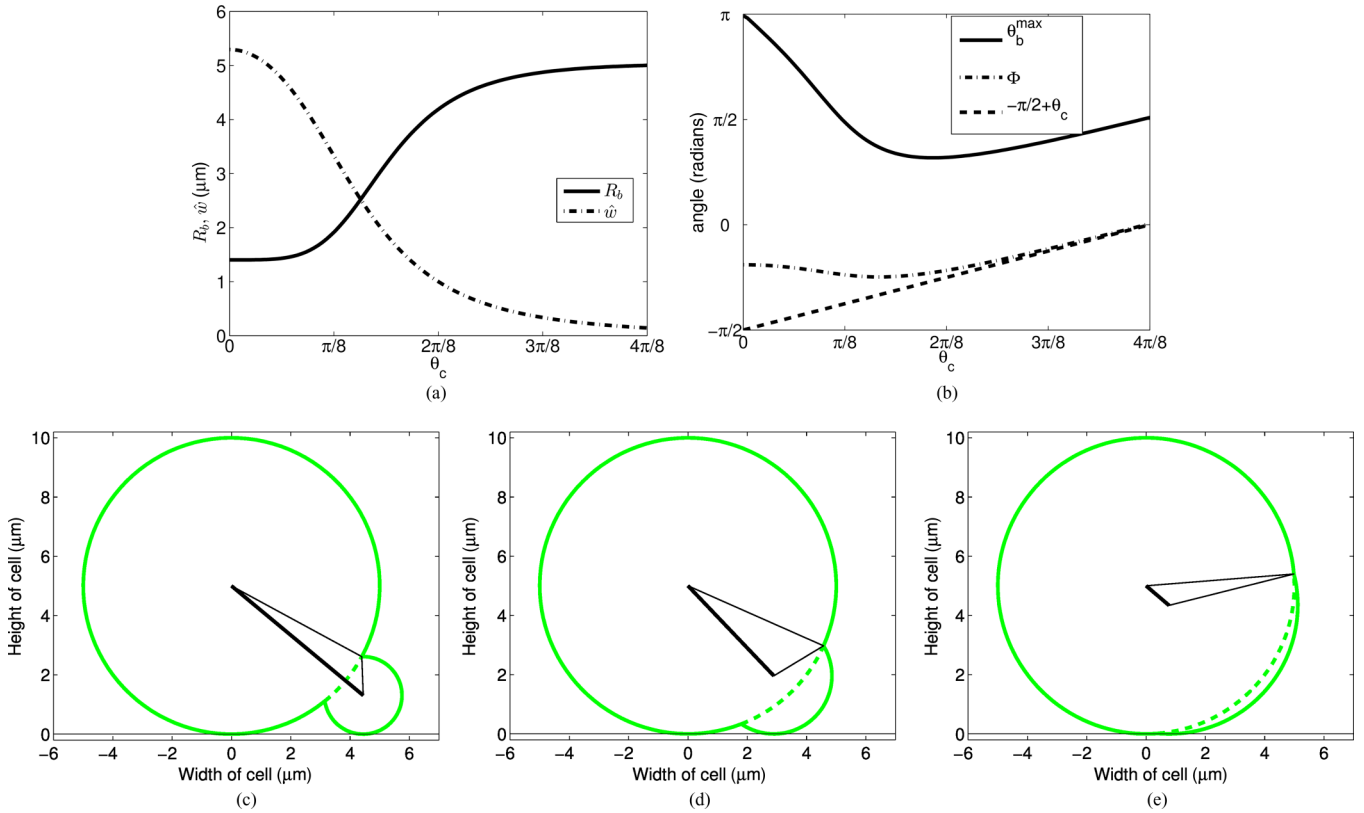

FIG. 12. Illustrating the influence of θ_c on (a) R_b and $\hat{w}$, produced through Eq. (29) and combining Eqs. (41) and (48), respectively; and (b) $\theta_b^{\max}$ and Φ, produced through Eq. (30) and Eq. (41), respectively. (c), (d), and (e) help demonstrate the trends seen in (a) and (b) as they are cell profiles that illustrate the maximum bleb extension, hence, $r_b = R_b$, $w = \hat{w}$, $\theta_b = \theta_b^{\max}$, and $\phi = \Phi$. The parameter values are the same as described in the caption of Fig. 6 and in (c), (d), and (e), $\theta_c = \pi/16$, $\pi/8$, and $\pi/4$, respectively.

to estimate one of the other parameters, then θ_c and ρ_c can be estimated from experiments. Further, it has been demonstrated previously [29,31] that μ only has a weak influence on the properties of the cell and, thus, can be fixed at its intermediate value of $\mu = 1/2$. Thus, we are left with estimating ΔP_0, A, and $C\kappa$. Although difficult, it is possible to estimate these parameters experimentally [35,36,43,44]. However, the results from this paper illustrate that only two of these three need be derived from data: the third can be predicted through the relationships generated in Sec. II. Even if only one of these parameters can be fixed through data we would still be able to generate a relationship concerning the dependencies of the other two. This would lead to at least a qualitative understanding of how the parameters may be correlated with each other and may even suggest parameter regions within which the two parameters must lie.

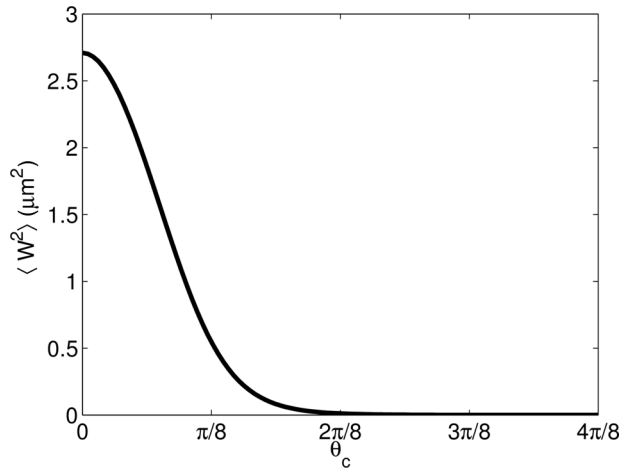

FIG. 13. Illustrating the relationship between θ_c and $\langle W^2 \rangle$, produced by combining Eqs. (29), (30), (41), (48), and (59). The parameter values are the same as in Fig. 6.

Our theoretical framework is able to capture the essential features of the blebbing motion, as it is able to predict parameter values that match experimental data. Moreover, we are able to encompass certain experimental perturbations, such as treatment with the methyl ester, L-NAME [24]. L-NAME acts a competitive inhibitor preventing the synthesis of nitric oxide, which has been highlighted as an important pathway in regular blebbing motion [13]. Critically, the blebs that are produced from L-NAME-treated cells are still viable and undergo the same extension and retraction phases; however, there are far fewer blebs in number (often only one at a time) and their neck angle, θ_c, is much wider. Specifically, wild-type cells are similar to those in Fig. 12(c), whereas L-NAME-treated cells have blebs much more like those seen in Fig. 12(d). Although we do not have specific data to compare with our results, we can at least qualitatively match the characteristics of the observations, namely that L-NAME-treated cell spread out in space much slower than

wild-type cells, which is consistent with the predictions from Fig. 13.

The results illustrated in Figs. 12 and 13 reinforce the findings of Woolley *et al.* [29], where it was argued that blebs with neck widths smaller than their maximum widths (known as small-necked-blebs) play an important role. Specifically, it was seen that small-necked-blebs were difficult to maintain as the forces acting on the cortex-membrane adhesions were large enough to cause the membrane to peel away from the cortex. As the membrane peels away from the cortex the neck width of the bleb increases, resulting in a cell profile similar to that of Fig. 12(d), rather than Fig. 12(c). Here, we offer an answer to an accompanying question, namely, since small-necked-blebs are hard to maintain, how critical is their contribution to motility? We find that if the bleb's neck is allowed to grow, the bleb's extension is significantly reduced. In turn, this leads to a dramatic reduction in the migration abilities of the cell. For the muscle stem cells that we are considering, this would suggest that they are not able to search and find damaged muscle as efficiently.

ACKNOWLEDGMENTS

A.G. acknowledges support from a Reintegration Grant under EC Framework VII. T.E.W. thanks the Mathematical Biosciences Institute (MBI) at Ohio State University for financially supporting this research through the National Science Foundation Grant No. DMS 1440386. T.E.W. also acknowledges financial support from St John's College, Oxford, and BBSRC Grant No. BKNXBKOO BK00.16.

APPENDIX: DERIVATION OF THE CHARACTERISTIC FUNCTION

The evolution equation of the cell's position is

$$P(x,y,n+1) = \int_0^{2\pi}\int_0^{\hat{w}} P[x - w\cos(\theta), y - w\sin(\theta), n] \times \frac{f(w)}{2\pi} dw d\theta. \tag{A1}$$

Equation (A1) can then be notionally solved by converting the integral into Cartesian coordinates and using Fourier transforms,

$$P(\boldsymbol{x},n) = \mathcal{F}^{-1}\left[\mathcal{F}\left(\frac{f(|\boldsymbol{x}|)}{2\pi|\boldsymbol{x}|}\right)^n\right], \tag{A2}$$

where we have used the initial condition $P(\boldsymbol{x},0) = \delta(|\boldsymbol{x}|)$ and the identity,

$$\mathcal{F}[\delta(|\boldsymbol{x}|)] = \int_{-\infty}^{\infty}\int_{-\infty}^{\infty} e^{-ik_1x - ik_2y}\delta(|\boldsymbol{x}|)dxdy = 1. \tag{A3}$$

Using Eq. (A2), we construct the characteristic function, or complex moment generating function, which will provide us with an analytical form for all of the moments of the probability density. The characteristic function is

$$\mathbb{E}_n(e^{it_1X+it_2Y}) = \int_{-\infty}^{\infty}\int_{-\infty}^{\infty} e^{it_1x+it_2y}P(x,y,n)dxdy. \tag{A4}$$

Critically, we notice that

$$\begin{aligned}\mathbb{E}_n(e^{it_1X+it_2Y}) &= F(P)(-t_1,-t_2)\\ &= \left[F\left(\frac{f(|\boldsymbol{x}|)}{2\pi|\boldsymbol{x}|}\right)(-t_1,-t_2)\right]^n,\end{aligned} \tag{A5}$$

where we have used Eq. (A2). Converting the equation back into polar coordinates, the Fourier transform becomes a finite Hankel transform [45],

$$\mathbb{E}_n(e^{it_1X+it_2Y}) = \left[\int_0^{\hat{w}} f(w)J_0(rt)dw\right]^n, \tag{A6}$$

where we have substituted $t = \sqrt{t_1^2+t_2^2} = |\boldsymbol{t}|$ and J_0 is the zeroth-order Bessel function of the first kind. Thus, in summary,

$$\begin{aligned}\mathbb{E}_n(X^{m_1}Y^{m_2}) &= (-i)^{m_1+m_2}\left.\frac{d^{m_1+m_2}}{dt_1^{m_1}dt_2^{m_2}}\right|_{\boldsymbol{t}=(0,0)}\\ &\quad\times\left[\int_0^{\hat{w}} f(w)J_0(wt)dw\right]^n.\end{aligned} \tag{A7}$$

Such results allow the evaluation of any moment for the analytical model as required.

[1] R. McLennan, L. Dyson, K. W. Prather, J. A. Morrison, R. E. Baker, P. K. Maini, and P. M. Kulesa, Multiscale mechanisms of cell migration during development: Theory and experiment, Development **139**, 2935 (2012).

[2] Y. Naparstek, J. Holoshitz, S. Eisenstein, T. Reshef, S. Rappaport, J. Chemke, A. Ben-Nun, and I. R. Cohen, Effector T lymphocyte line cells migrate to the thymus and persist there, Nature **300**, 262 (1982).

[3] A. P. Singh, U. Schach, and C. Nüsslein-Volhard, Proliferation, dispersal and patterned aggregation of iridophores in the skin prefigure striped colouration of zebrafish, Nat. Cell. Biol. **16**, 607 (2014).

[4] P. L. Townes and J. Holtfreter, Directed movements and selective adhesion of embryonic amphibian cells, J. Exp. Zool. **128**, 53 (1955).

[5] F. A. Meineke, C. S. Potten, and M. Loeffler, Cell migration and organization in the intestinal crypt using a lattice-free model, Cell Prolif. **34**, 253 (2001).

[6] N. A. Wright and M. Alison, *The Biology of Epithelial Cell Populations*, Vol. 1 (Oxford University Press, New York, 1984).

[7] J. P. Heath, Epithelial cell migration in the intestine, Cell. Biol. Int. **20**, 139 (1996).

[8] G. Oster and A. S. Perelson, Cell Protrusions, In *Frontiers in Mathematical Biology*, Vol. 100, edited by S. A. Levin (Springer, Berlin/Heidelberg, 1994), pp. 53–78.

[9] W. H. Goldmann, Mechanical aspects of cell shape regulation and signaling, Cell. Biol. Int. **26**, 313 (2002).

[10] J. Lee, A. Ishihara, and K. Jacobson, How do cells move along surfaces? Trends Cell Biol. **3**, 366 (1993).

[11] G. T. Charras, A short history of blebbing, J. Micros. **231**, 466 (2008).
[12] G. T. Charras, M. Coughlin, T. J. Mitchison, and L. Mahadevan, Life and times of a cellular bleb, Biophys. J. **94**, 1836 (2008).
[13] H. Collins-Hooper, T. E. Woolley, L. Dyson, A. Patel, P. Potter, R. E. Baker, E. A. Gaffney, P. K. Maini, P. R. Dash, and K. Patel, Age-related changes in speed and mechanism of adult skeletal muscle stem cell migration, Stem Cells **30**, 1182 (2012).
[14] H. Blaser, M. Reichman-Fried, I. Castanon, K. Dumstrei, F. L. Marlow, K. Kawakami, L. Solnica-Krezel, C. P. Heisenberg, and E. Raz, Migration of zebrafish primordial germ cells: A role for myosin contraction and cytoplasmic flow, Dev. Cell. **11**, 613 (2006).
[15] E. Sahai and C. J. Marshall, Differing modes of tumour cell invasion have distinct requirements for Rho/ROCK signaling and extracellular proteolysis, Nat. Cell. Biol. **5**, 711 (2003).
[16] O. T. Fackler and R. Grosse, Cell motility through plasma membrane blebbing, J. Cell. Biol. **181**, 879 (2008).
[17] H. Keller and P. Eggli, Protrusive activity, cytoplasmic compartmentalization, and restriction rings in locomoting blebbing Walker carcinosarcoma cells are related to detachment of cortical actin from the plasma membrane, Cell. Motil. Cytoskel. **41**, 181 (1998).
[18] C. C. Cunningham, Actin polymerization and intracellular solvent flow in cell surface blebbing, J. Cell Biol. **129**, 1589 (1995).
[19] G. Charras and E. Paluch, Blebs lead the way: How to migrate without lamellipodia, Nat. Rev. Mol. Cell Biol. **9**, 730 (2008).
[20] J. Y. Tinevez, U. Schulze, G. Salbreux, J. Roensch, J. F. Joanny, and E. Paluch, Role of cortical tension in bleb growth, Proc. Natl. Acad. Sci. USA **106**, 18581 (2009).
[21] J. Dai and M. P. Sheetz, Membrane tether formation from blebbing cells, Biophys. J. **77**, 3363 (1999).
[22] J. Mercer and A. Helenius, Vaccinia virus uses macropinocytosis and apoptotic mimicry to enter host cells, Science **320**, 531 (2008).
[23] M. A. Gonda, S. A. Aaronson, N. Ellmore, V. H. Zeve, and K. Nagashima, Ultrastructural studies of surface features of human normal and tumor cells in tissue culture by scanning and transmission electron microscopy, J. Natl. Cancer Inst. **56**, 245 (1976).
[24] A. Otto, H. Collins-Hooper, A. Patel, P. R. Dash, and K. Patel, Adult skeletal muscle stem cell migration is mediated by a blebbing/amoeboid mechanism, Rejuv. Res. **14**, 249 (2011).
[25] D. W. Dorward, C. F. Garon, and R. Judd, Export and intercellular transfer of DNA via membrane blebs of Neisseria gonorrhoeae, J. Bacteriol. **171**, 2499 (1989).
[26] W. Strychalski and R. D. Guy, A computational model of bleb formation, Math. Med. Biol. **30**, 115 (2012).
[27] J. Hu, *Mathematical Modeling and Analysis of in vitro Actin Filament Dynamics and Cell Blebbing*, PhD. thesis, Univeristy of Minnesota 2009.
[28] M. Tozluoğlu, A. L. Tournier, R. P. Jenkins, S. Hooper, P. A. Bates, and E. Sahai, Matrix geometry determines optimal cancer cell migration strategy and modulates response to interventions, Nat. Cell. Biol. **15**, 751 (2013).
[29] T. E. Woolley, E. A. Gaffney, J. M. Oliver, S. L. Waters, R. E. Baker, and A. Goriely, Global contraction or local growth, bleb shape depends on more than just cell structure, J. Theor. Biol. **380**, 83 (2015).
[30] T. E. Woolley, E. A. Gaffney, and A. Goriely, Membrane shrinkage and cortex remodelling are predicted to work in harmony to retract blebs, Roy. Soc. Open Sci. **2**, 150184 (2015).
[31] T. E. Woolley, E. A. Gaffney, J. M. Oliver, R. E. Baker, S. L. Waters, and A. Goriely, Cellular blebs: Pressure-driven, axisymmetric, membrane protrusions, Biomech. Model. Mechan. **13**, 463 (2014).
[32] T. E. Woolley, E. A. Gaffney, S. L. Waters, J. M. Oliver, R. E. Baker, and A. Goriely, Three mechanical models for blebbing and multi-blebbing, IMA J. Appl. Math. **79**, 636 (2014).
[33] B. Maugis, J. Brugués, P. Nassoy, N. Guillen, P. Sens, and F. Amblard, Dynamic instability of the intracellular pressure drives bleb-based motility, J. Cell. Sci. **123**, 3884 (2010).
[34] E. A. Evans and R. Skalak, *Mechanics and Thermodynamics of Biomembranes* (CRC Press, Boca Raton, FL, 1980).
[35] D. Liu, L. Ge, F. Wang, H. Takahashi, D. Wang, Z. Guo, S. H. Yoshimura, T. Ward, X. Ding, K. Takeyasu, and X. Yao, Single-molecule detection of phosphorylation-induced plasticity changes during ezrin activation, FEBS Lett. **581**, 3563 (2007).
[36] M. P. Sheetz, J. E. Sable, and H. G. Döbereiner, Continuous membrane-cytoskeleton adhesion requires continuous accommodation to lipid and cytoskeleton dynamics, Annu. Rev. Biophys. Biomol. Struct. **35**, 417 (2006).
[37] T. Bihr, U. Seifert, and A.-S. Smith, Multiscale approaches to protein-mediated interactions between membranesrelating microscopic and macroscopic dynamics in radially growing adhesions, New J. Phys. **17**, 083016 (2015).
[38] T. Bihr, U. Seifert, and A.-S. Smith, Nucleation of Ligand-Receptor Domains in Membrane Adhesion, Phys. Rev. Lett. **109**, 258101 (2012).
[39] F. Chamaraux, S. Fache, F. Bruckert, and B. Fourcade, Kinetics of Cell Spreading, Phys. Rev. Lett. **94**, 158102 (2005).
[40] B. D. Hughes, *Random Walks and Random Environments* (Clarendon Press, Oxford, UK, 1996).
[41] J. A. Nichol and O. F. Hutter, Tensile strength and dilatational elasticity of giant sarcolemmal vesicles shed from rabbit muscle, J. Phys. **493**, 187 (1996).
[42] C. Pozrikidis, Effect of membrane bending stiffness on the deformation of capsules in simple shear flow, J. Fluid. Mech. **440**, 269 (2001).
[43] Y. C. Fung, *Biomechanics: Mechanical Properties of Living Tissues* (Springer, New York, 1993).
[44] M. F. Ashby, L. J. Gibson, U. Wegst, and R. Olive, The mechanical properties of natural materials. I. Material property charts, Proc. R. Soc. London A **450**, 123 (1995).
[45] R. Bracewell, *The Fourier Transform and Its Applications* (McGraw Hill, New York, 1965).